Gong *et al. Biochar* (2026) 8:110
https://doi.org/10.1007/s42773-026-00624-w

Biochar

ORIGINAL RESEARCH **Open Access**

Hydrolysis time-controlled pore and defect engineering in nanocellulose-derived biochar for enhanced ethylene glycol sensing

Yichen Gong[1,3], Cong Liang[1,3], Qihua Sun[2], Ping Hu[2,3], Yan Li[1,3], Junxi Cheng[1,3], Chang Liu[1,3], Bing Gao[1,3], Hua Zhuo[4*] and Zhaofeng Wu[1,3*]

Abstract

This study presents a hydrolysis time-mediated strategy for engineering the pore and defect structure of biochar derived from lavender straw nanocellulose. The biochar obtained at the optimal hydrolysis duration of 3 h (CLN-3) exhibits a developed mesoporous network (46.36 $m^2\ g^{-1}$) and abundant oxygen vacancies, leading to exceptional ethylene glycol (EG) sensing performance at room temperature: a high response of 17,576.67%, a low detection limit of 0.36 ppm, and stable operation over 40 days. Density functional theory (DFT) calculations reveal that calcium doping enhances the adsorption energy of EG from − 0.13674 eV to − 0.39508 eV, facilitating interfacial charge transfer. This work provides a green and controllable route to transform agricultural waste into high-performance sensing materials.

Highlights

- A controllable hydrolysis method transforms nanocellulose into functional biochar with tuned pores and defects.
- The best-performing biochar exhibits exceptional sensitivity, a low detection threshold, and stable long-term operation for EG sensing.
- Hydrolysis time is identified as the key to tailoring biochar properties, enabling the design of high-performance gas sensors.

Keywords Hydrolysis time, Pore structure, Defect engineering, Nanocellulose-derived biochar, EG sensing

---

*Correspondence:
Hua Zhuo
zh830011@163.com
Zhaofeng Wu
wuzf@xju.edu.cn
Full list of author information is available at the end of the article

Graphical Abstract

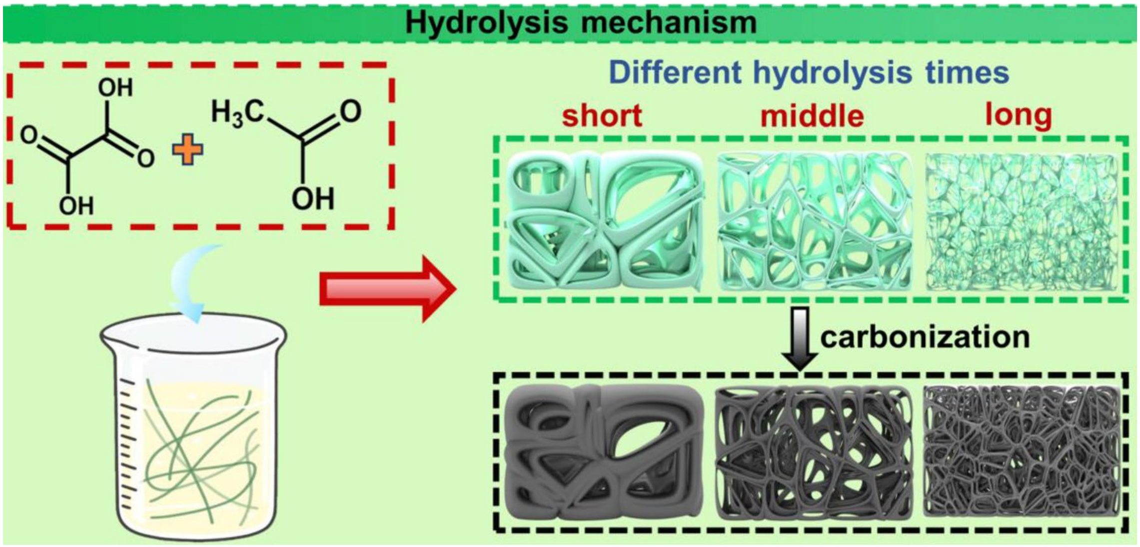

1 Introduction

Biochar materials exhibit broad application prospects in volatile organic compound (VOC) detection due to their tunable pore structures and surface chemical properties (Fang et al. 2026; Jin et al. 2025; Liu et al. 2025a). Among these, ethylene glycol (EG), a typical polar organic solvent with a boiling point of 197.3 °C, is widely used in the synthesis of polyesters and in the production of antifreeze. However, its toxicity may suppress the central nervous system and cause multiple organ failure (Ibrahim et al. 2019; Su et al. 2020). Therefore, developing high-performance EG sensors with low detection limits holds significant practical importance.

In recent years, plant fiber-derived nanocellulose has emerged as a promising biochar precursor, owing to its abundant surface hydroxyl groups, high aspect ratio, and excellent thermal stability—features that favor the construction of hierarchical porous networks and efficient gas adsorption (Chauhan et al. 2025; Dong et al. 2025a; Hernandez-Ortega et al. 2025). Oxalic acid, known for its environmental friendliness, is widely used to remove lignin and hemicellulose while preserving cellulose crystallinity (Vinod et al. 2021). Among plant-derived feedstocks, lavender straw, an underutilized agricultural waste from Xinjiang, is selected for its structural and economic merits for low-cost, high-value conversion (Liu et al. 2025b). Compared with common biomass residues (rice straw, wheat straw, and corn cob), it features a loose fibrous structure, balanced cellulose/lignin ratio, and intrinsic calcium content within the optimal range for gas-sensing applications. Its higher calcium content facilitates mild hydrolysis for nanocellulose extraction, while avoiding structural collapse of the derived biochar (Chaloupkova et al. 2021; Copenhaver et al. 2022; Ercan et al. 2023; Yahya et al. 2023; Xu et al. 2024). Further incorporation of acetic acid facilitates the establishment of a synergistic hydrolysis system, enabling effective regulation of defect structures during biocharization and promoting the formation of specific oxygen vacancies and edge defects. This enhances adsorption activity toward polar molecules such as EG (Holilah et al. 2022; Wang et al. 2023). Although acid hydrolysis pretreatment is a key strategy for optimizing biomass composition and enhancing biochar performance, current understanding remains limited regarding how critical pretreatment parameters—particularly hydrolysis time—influence the microstructure (e.g., defect types, concentrations, and distributions) and surface chemistry of the final biochar (Eom et al. 2019; Wang et al. 2025a). This knowledge gap constrains the precise regulation of gas-sensing performance in biochar-based sensing materials.

This study employs an oxalic acid–acetic acid binary hydrolysis system to investigate how hydrolysis time modulates the pore and defect structures of lavender straw nanocellulose-derived biochar. Hydrolysis duration governs the degree of cellulose dissociation, directly regulating the final porous structure and gas-sensing performance of the biochar. Moderate hydrolysis for 3 h yields biochar with a well-developed mesoporous network, high specific surface area, and abundant oxygen vacancies, while insufficient or excessive hydrolysis causes structural degradation and compromised performance. Combined with DFT calculations, we reveal that intrinsic calcium doping and pre-adsorbed oxygen synergistically enhance EG adsorption and interfacial charge transfer. This work clarifies the hydrolysis time-biochar gas-sensing structure-performance relationship, offers a green, controllable strategy for developing high-performance biochar-based gas sensors, and enables high-value conversion of underutilized agricultural biomass waste.

2 Experimental section

2.1 Materials and reagents

All chemical reagents used in this study are of analytical grade. Sodium hydroxide (NaOH), oxalic acid ($C_2H_2O_4$), acetic acid (CH_3COOH), anhydrous ethanol, and sodium hypochlorite (NaClO) were purchased from Tianjin Beilian Fine Chemical Development Co., Ltd. Other chemical standards include hydrazine (N_2H_4), ammonia solution (NH_3), formaldehyde (CH_2O), aniline (C_6H_7N), methanol (CH_4O), EG ($C_2H_6O_2$), ethanol (C_2H_6O), and acetone (C_3H_6O), all purchased from Sinopharm Chemical Reagent Co., Ltd. Hydrogen peroxide (H_2O_2) was purchased from Aladdin Reagent Co., Ltd. The biomass feedstock lavender straw was collected as agricultural residue from Huocheng County, Xinjiang.

2.2 Preparation of CLN-X

As illustrated in Fig. 1, nanocellulose precursors (LN-X) were derived from lavender stems via sequential purification and oxalic acid/glacial acetic acid hydrolysis (1:1, m/m, 90 °C, 1–5 h), followed by freeze-drying. TGA analysis (Fig. S1) optimized carbonization at 450 °C, yielding CLN-X (X = hydrolysis time). Detailed preparation steps are available in Text S1.

2.3 Material characterization

The samples' characteristics were comprehensively assessed and examined through a range of complementary characterization techniques. Additional information on instrument parameters and detailed procedures is provided in Text S2.

2.4 Calculation method

DFT calculations were performed using the VASP package with standard computational settings. Detailed

Fig. 1 CLN-X preparation process flowchart

calculation parameters and procedures are provided in Supplementary Text S3.

2.5 Preparation and sensing test

Gas sensing performance was tested at room temperature via a static volumetric system. CLN-X sensors were fabricated by drop-casting: CLN-X powder was uniformly dispersed in deionized water (1:3 mass ratio) to form a homogeneous slurry, 10 μL of which was drop-cast onto Ag/Pd (95:5, m/m) interdigitated electrodes on an Al_2O_3 ceramic substrate (13 × 7 × 0.635 mm), and then dried at room temperature for 24 h to form a uniform, compact sensing layer (Fig. S2a–c). Detailed fabrication and test protocols are provided in Text S4.

3 Results and discussion

3.1 Morphology and structure of materials

The morphological evolution of the nanocellulose precursors with hydrolysis time was tracked by TEM (Fig. 2a–c). Short-term hydrolysis (1 h) led to surface roughening, while an optimal 3-h treatment resulted in complete dissociation into uniformly sized nanofibers with a well-ordered mesoporous architecture. In contrast, over-hydrolysis caused severe structural fragmentation (Kamboj et al. 2025; Saupi et al. 2025; Sawatdee et al. 2025; Xue et al. 2025). The corresponding carbonized samples (CLN-X) showed that only the optimally hydrolyzed precursor (CLN-3) formed a continuous mesoporous network upon carbonization, which is critical for gas sensing. Elemental mapping (Fig. 2d) confirmed the homogeneous distribution of C, O, and Ca in CLN-3. The source of this calcium was traced to the lavender straw feedstock itself, as indicated by ICP-MS analysis (Table S1), which measured a Ca content of approximately 0.98 wt% in the raw biomass. These results demonstrate that the calcium doping observed in CLN-3 originates naturally from the agricultural residue and was not introduced externally during synthesis. (Cheng et al. 2019; Lavarack et al. 2002; Shankar and Rhim 2016; Sun and Lin 2010). To validate our feedstock selection, we

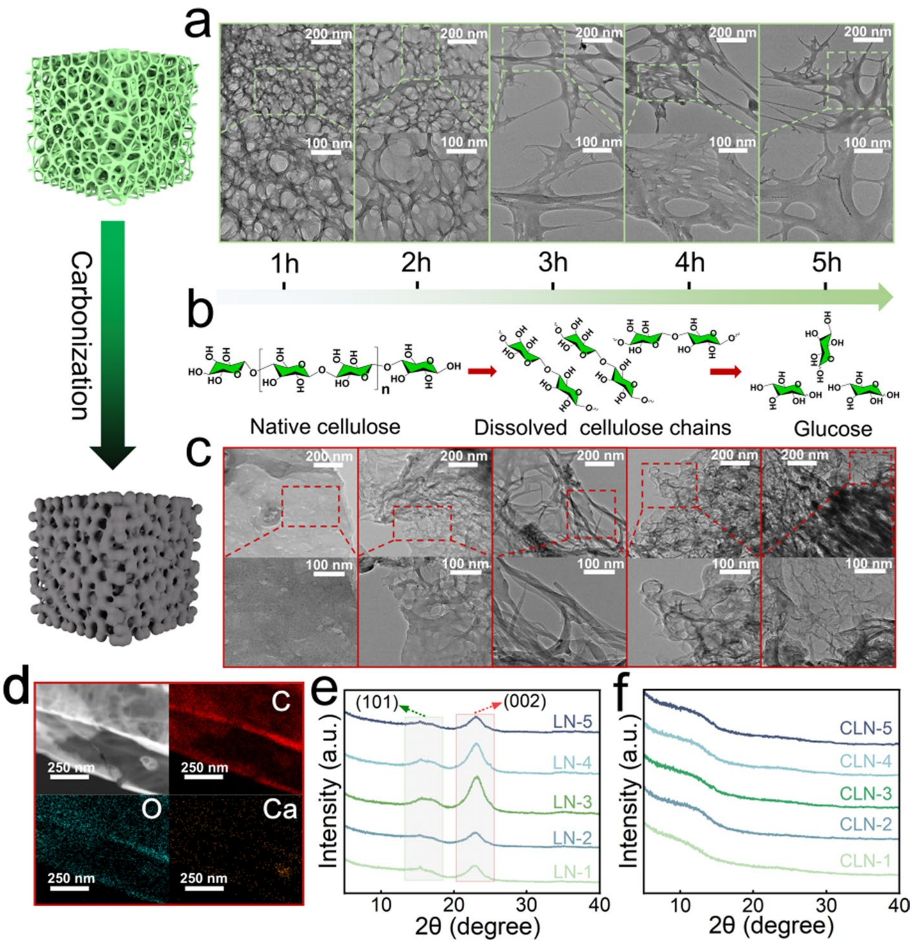

Fig. 2 **a** TEM images of nanocellulose hydrolyzed for 1–5 h; **b** Schematic of cellulose chain cleavage; **c** Mesostructure of carbonized CLN-X; **d** Elemental mapping of CLN-3; **e** XRD patterns of pristine nanocellulose (LN-X); **f** Amorphous XRD features of carbonized CLN-X

compared the calcium content of lavender straw with common biomass residues (Table S2). Its Ca content (0.9823 at.%) falls within the typical mineral range, verifying its suitability as a natural self-doping precursor. The crystalline structure of the precursors was analyzed by XRD (Fig. 2e). All LN-X samples showed characteristic cellulose I peaks. Notably, the intensity of the (002) diffraction exhibited a clear non-monotonic trend, peaking at LN-3. This indicates that moderate hydrolysis (1–3 h) effectively removes amorphous regions and enhances crystallinity, whereas excessive hydrolysis degrades the crystalline order (Bai et al. 2024; Chagas et al. 2023; Hou et al. 2025; Ike and Wal 2024; Pratiwi et al. 2023). The corresponding carbonized samples are shown in Fig. 2f.

Hydrolysis time-regulated non-monotonic variation in precursor crystallinity governs biochars' defect and pore structures through kinetically modulated cellulose chain cleavage (complete kinetic model/derivation in Text S5; pseudo-first-order fitting results in Fig. S3). A core kinetic correlation $\frac{C}{C_0} = \frac{CrI_t}{CrI_{max}}$ quantifies this effect, where C_0 is the initial glycosidic bond concentration in cellulose crystalline regions, CrI_t is the crystallinity after t hours of hydrolysis, and $CrI_{max} = 80.60\%$ (maximum crystallinity of CLN-3). Fitting results identify two stages: selective etching (1–3 h, $k_1 = 0.0393\ h^{-1}$, $R^2 = 0.984$) preferentially removing amorphous regions, and over-etching (3–5 h, $k_2 = 0.0327\ h^{-1}$, $R^2 = 0.851$) damaging crystalline structures. Moderate hydrolysis (3 h) maximizes LN-X's crystallinity (80.60%, Table S3) and thermal stability (262.8 °C, Fig. S1), enabling controlled cellulose chain cleavage during carbonization to form a well-developed mesoporous network and optimized O_C/O_V ratio. In contrast, insufficient hydrolysis (1–2 h) leaves residual amorphous regions, while excessive hydrolysis (4–5 h) disrupts crystalline order, and both cause unbalanced defect distribution and compromised pore development. Notably, after carbonization, all CLN-X samples exhibited nearly identical broad XRD patterns (Fig. 2f), which correspond to the (002) and (100) crystal planes of disordered carbon. This result confirms that the overall highly amorphous structure of the final biochar is independent of the initial crystallinity of the cellulose precursors (Biswas et al. 2022; Yang et al. 2020). However, as revealed by the hydrolysis kinetic model in Supplementary Text S5, the precursor crystallinity tuned by hydrolysis time dominates the pyrolysis behavior during carbonization by regulating the thermal stability of cellulose precursors, which further determines the pore structure development and surface defect evolution of the final biochar. Three hours of moderate hydrolysis represents the critical condition for achieving the optimal material structure: this treatment maximizes the cellulose crystallinity (80.60%), constructs the most developed mesoporous network with a maximum specific surface area of 46.36 $m^2\ g^{-1}$, and modulates an optimal ratio of chemisorbed oxygen (O_C) to oxygen vacancies (O_V). This unique structural combination fully balances the availability of effective active sites for gas adsorption and the surface redox activity, which serves as the core structural origin for the superior EG sensing performance of CLN-3.

The chemical structural evolution during carbonization was analyzed by Fourier transform infrared (FTIR) spectroscopy (Fig. 3a). Following carbonization, the intensities of most characteristic absorption bands associated with cellulose functional groups were markedly attenuated. A broad absorption band centered around 3400 cm^{-1} is assigned to O–H stretching vibrations of residual hydroxyl groups (Yang et al. 2020). The peaks near 2900 cm^{-1} and 1044 cm^{-1} correspond to C–H and C–O stretching vibrations, respectively (Biswas et al. 2022). Weak but discernible signals at approximately 1629 cm^{-1} and 1450 cm^{-1} are attributed to C=C stretching vibrations within the aromatic skeletal structure of residual lignin (Biswas et al. 2022; Hayashi et al. 2025; Stan et al. 2023). The persistence of these oxygen-containing functional groups after carbonization indicates their high thermal stability. It suggests their potential role as active sites for enhancing surface reactivity in the biochar material (Gao and Zhang 2025; Mohamed et al. 2025; Smith-Craven et al. 2024). Raman spectroscopy of the CLN-X biochars (Fig. 3b) showed characteristic D (~ 1350 cm^{-1}) and G (~ 1580 cm^{-1}) bands, corresponding to structural defects and sp^2-hybridized graphitic carbon, respectively (Antil et al. 2025; Smith et al. 2016). The I_D/I_G ratio ranged from 0.55 to 0.74, confirming a highly disordered, amorphous carbon structure. No systematic variation in I_D/I_G with hydrolysis time was observed, indicating that precursor crystallinity had little influence on the final graphitization degree under the given carbonization conditions (Chen et al. 2017; Ferrari and Basko 2013; Ferrari and Robertson 2000; Meunier et al. 2022). This is consistent with XRD results, where broad features around 24° and 43°replaced cellulose peaks, further confirming the amorphous nature of the biochars (Ferrari and Robertson 2000; Franklin 1951; Mubari et al. 2022). UV–Vis spectra (Fig. 3c) show hydrolysis time-dependent intensity variations, with Tauc plots (Fig. 3d) yielding optical band gaps of 0.80–1.28 eV (non-monotonic trend for CLN-1 to CLN-5). This indicates that hydrolysis tunes defect states via precursor dissociation, and the inverse correlation between band gap and gas response suggests that sensing performance is dominated by pore structure and surface area rather than electronic properties.

The surface chemistry of biocharized lavender nanocellulose (CLN-X) was analyzed using XPS, with a focus

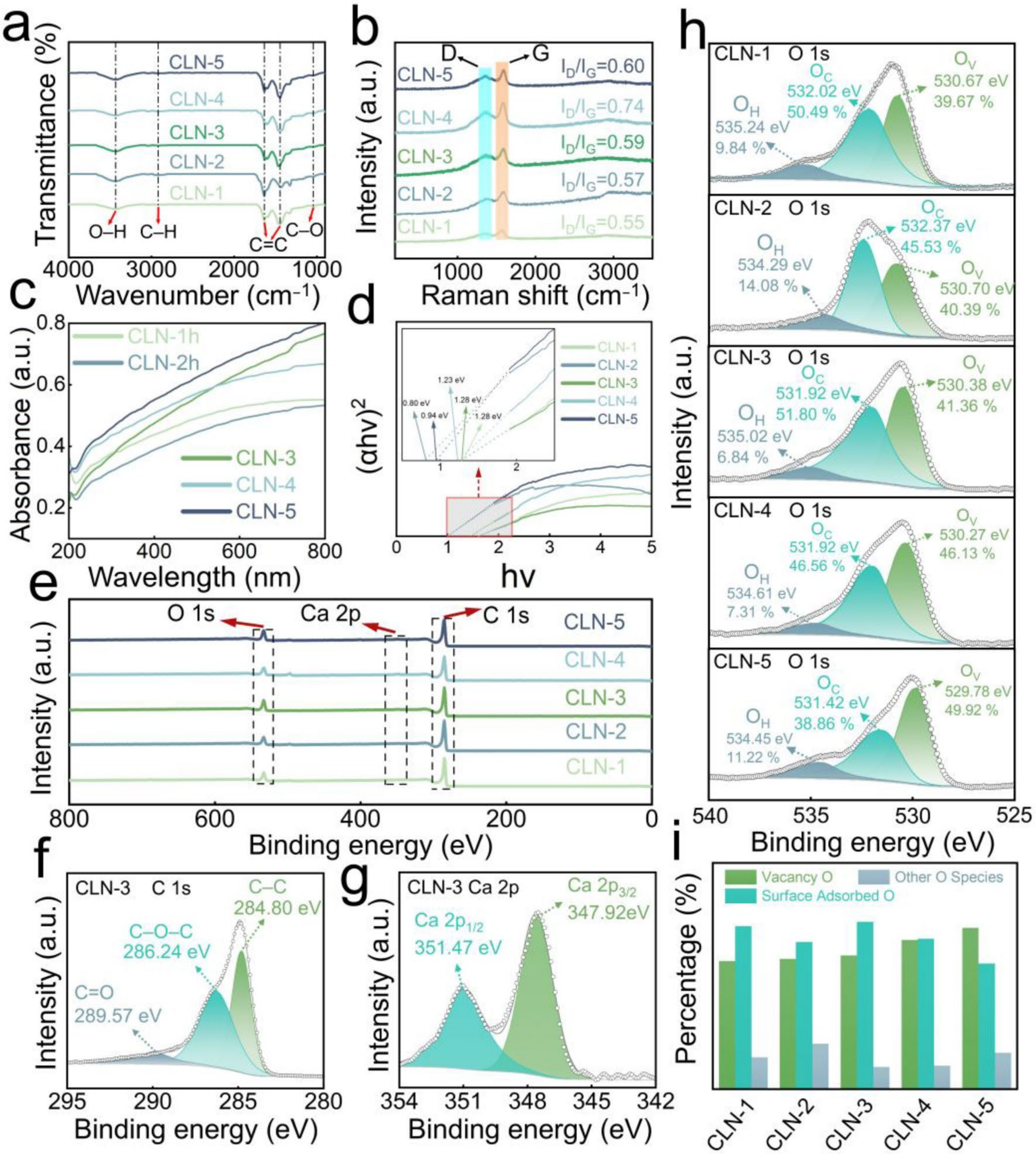

Fig. 3 Surface chemical and structural characterization: **a** FT-IR spectrum. **b** Raman spectrum revealing I_D/I_G defect density; **c** Ultraviolet–visible Spectra; **d** Tauc plots of CLN-X; **e**XPS spectrum of CLN-X; **f** C 1 s XPS spectrum; **g** Ca 2p XPS; **h** O 1 s XPS spectrum of CLN-X; **i** The relative percentage content of O_V, O_C, and other O species

on oxygen-containing functional groups. Survey spectra (Fig. 3e) indicate the presence of C, O, and Ca. High-resolution C 1 s spectra (Figs. 3f–h and S4) show peaks corresponding to C–C (284.80 eV), C–O–C (286.04 eV), and C=O (289.03 eV) (Choudhary et al. 2025; Li et al. 2025; Liu et al. 2025c). The O 1 s spectrum was deconvoluted into three components: oxygen vacancies (O_V, 530.38 eV), chemisorbed oxygen species (O_C, 531.92 eV), and hydroxyl groups (O_H, 535.02 eV) (Sun et al. 2025; Wang et al. 2025b). The O_V content increased from 39.67% (CLN-1) to 49.92% (CLN-5) with the hydrolysis time. CLN-3 exhibited the highest O_C content (51.8%), which correlated with its superior gas response and suggested an optimal O_C concentration for sensing. The O_H content remained stable (7–14%). The Ca 2p spectrum exhibited a doublet at 347.92 eV and 351.47 eV, indicating

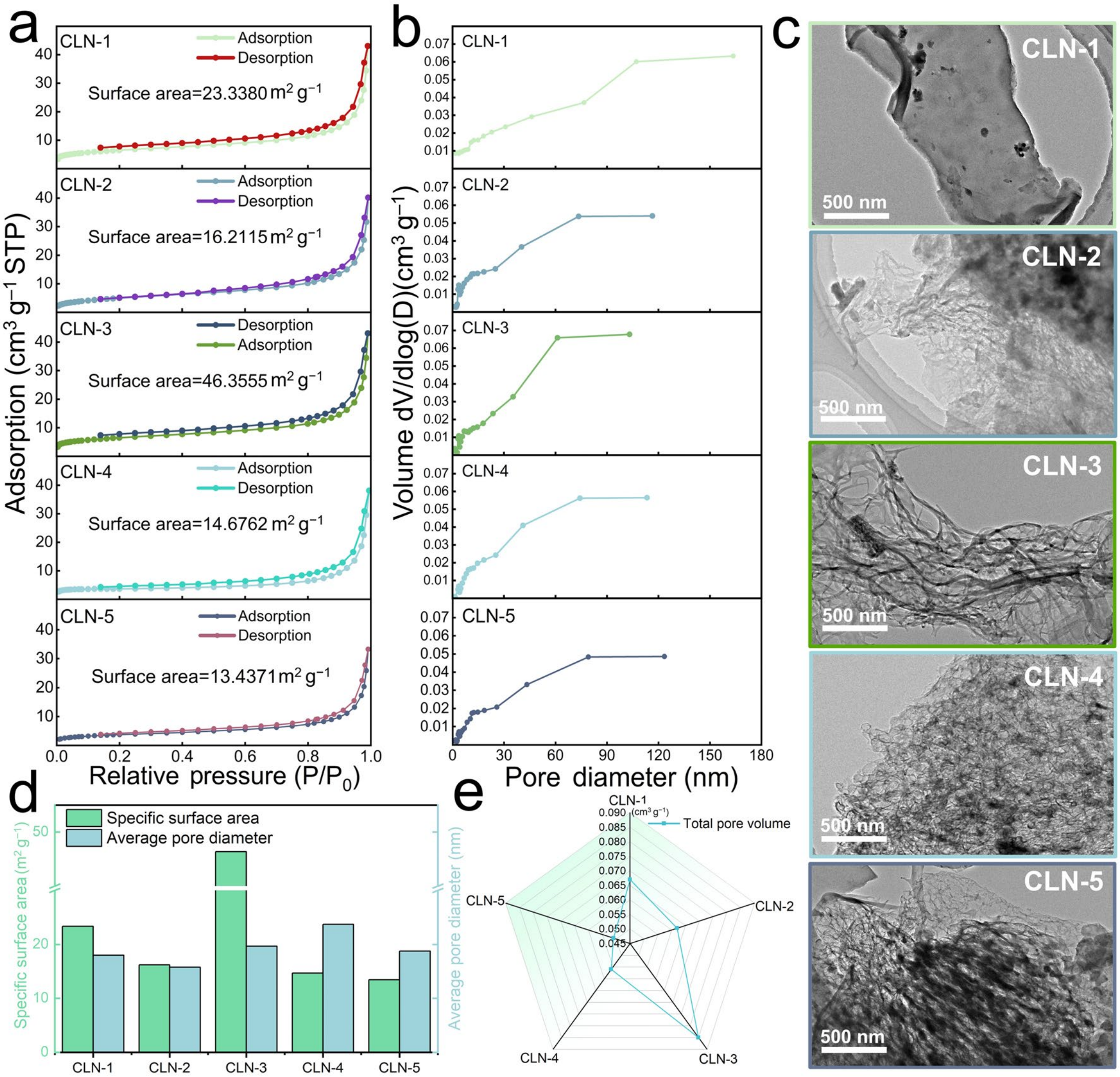

Fig. 4 Pore structure and particle size analysis: **a** Type IV nitrogen adsorption–desorption isotherm of CLN-X; **b** Pore size distribution of CLN-X; **c** TEM morphology comparison of CLN-X; **d** Specific surface area and average pore diameter of CLN-X; **e** Total pore volume of CLN-X, highlighting CLN-3's optimal porosity

the presence of oxidized calcium species (e.g., $CaCO_3$/CaO) (Shi et al. 2014; López et al. 2022), which may serve as natural templates or catalytic sites during biocharization. Figure 3h and 3i indicate that prolonged hydrolysis in the CLN-X series transforms the surface oxygen chemistry from a predominance of adsorbed oxygen (O_C) to a predominance of oxygen vacancies (O_V), with O_C reaching its peak at CLN-3. The increase in O_V enhances gas adsorption and charge transfer, while O_C participates in surface redox reactions (Fang et al. 2024). Combined with XRD and Raman data, this confirms that hydrolysis effectively modulates surface reactivity. The optimized O_C/O_V balance synergistically improves surface chemistry, laying the foundation for developing high-performance gas sensors.

Figure 4 illustrates the structural evolution of biochars with hydrolysis time. N_2 physisorption isotherms (Fig. 4a) confirm a mesoporous structure in all samples. CLN-3 possesses the highest specific surface area (46.36 m^2 g^{-1}), significantly exceeding those of CLN-1 (23.34), CLN-2 (16.21), CLN-4 (14.68), and CLN-5 (13.44 m^2 g^{-1}), which favors gas adsorption (Long et al. 2016; Yuan et al. 2019, 2022). While pore size distributions are alike (Fig. 4b), CLN-3 shows a sharper peak at smaller pores, indicating a more developed porous network. Microscopy (Fig. 4c) confirms these trends.

CLN-3 features an interwoven, open nanofiber network, while CLN-1 and CLN-2 have larger bundles and limited porosity, and CLN-4/5 show agglomeration and densification. This morphology is consistent with pore structure data (Fig. 4d, e): CLN-3 has the highest specific surface area and total pore volume, attributed to its well-developed porous network, while other samples have lower values due to incomplete pore formation or structural collapse. As shown in Fig. S5, TEM and statistical size analysis were employed to characterize particle morphology and dimensions, avoiding the spherical particle assumption inherent in DLS measurements. CLN-3 displays an open nanofiber network with a narrow particle size distribution (~ 12–15 nm), indicating well-controlled fiber dissociation. CLN-1/2 exhibit larger bundled structures, while CLN-4/5 show agglomeration, consistent with insufficient or excessive hydrolysis, respectively.

3.2 Gas sensing investigations of the samples

The gas sensing performance of the CLN-X series was evaluated at a constant bias of 4 V. The sensors were sequentially exposed to multiple analytes, including H_2O_2, CH_2O, N_2H_4, $C_2H_6O_2$, NH_3, $C_6H_5NH_2$, C_3H_6O, CH_3OH, and C_2H_5OH. The current signals were normalized to obtain dynamic response curves. As shown in Figs. 5 and S6, the CLN-X materials exhibit a markedly enhanced response to EG, consistent with prior reports (Li et al. 2024). Figure 5a compares the transient responses of CLN-1 to CLN-5 toward four representative gases (H_2O_2, CH_2O, N_2H_4, $C_2H_6O_2$). This response strongly depends on hydrolysis time: the signal intensity of CLN-3 is significantly higher than that of CLN-1, CLN-2, CLN-4, and CLN-5. A typical response/recovery curve of CLN-3 to 500 ppm EG (Fig. 5b) gives $T_{res} = 69.75$ s and $T_{rec} = 56.32$ s; the relatively slow kinetics may arise from the higher activation barrier for EG oxidation by pre-adsorbed oxygen. Across 100–400 ppm (Fig. 5c, d), the response exhibits excellent linearity ($R^2 = 0.992$), indicating reliable quantitative capability. The calculated detection limit is 0.36 ppm based on the linear fit slope and baseline noise.

Figure 6 summarizes the gas-sensing performance and key physicochemical properties of the CLN series. Comparative analysis (Fig. 6a) shows that CLN-3, obtained after 3 h of hydrolysis, possesses both the highest adsorbed-oxygen content and the largest specific surface area, and these structural advantages explain its superior sensing capability. Accordingly, CLN-3 delivers a significantly stronger response to EG than the other samples, which correlates well with its oxygen-rich surface and developed porous network. Furthermore, the sensor showed excellent cyclic stability (Fig. 6b) and maintained consistent signals during a 40-day test (Fig.6d), highlighting its reliable repeatability and long-term stability. In the comparison of response and response/recovery times for four gases (Fig. 6c), CLN-3 further demonstrated dual advantages of high responsiveness and rapid kinetics. Quantitative analysis revealed that its response to EG reached 17,576.67%, significantly higher than its responses to H_2O_2 (78.39%), CH_2O (533.75%), and N_2H_4 (467.40%), demonstrating outstanding selectivity. The CLN-3 sensor in this work realizes efficient room-temperature (RT) detection of EG, with faster response/recovery speeds, excellent repeatability and long-term stability relative to reported sensors. As shown in Table 1, CLN-3 delivers a nearly unchanged response after 40 days of testing and exhibits negligible attenuation over 10 consecutive cycles toward 500 ppm EG, outperforming most reported EG sensing materials. In contrast, conventional EG sensors usually require high operating temperatures, which greatly limits their applications in wearable devices and industrial inspection.

Based on the humidity response rules obtained from the static humidity sensing test system (Fig. S7), Fig. 7a illustrates the moisture-sensing mechanism of the CLN-3 biochar layer. Its response originates from the porous structure, surface functional groups (–OH, –COOH), and carbon defects. Under low humidity, water molecules chemically adsorb onto these groups via hydrogen bonding or coordination. An applied electric field enhances proton dissociation, promoting water dissociation ($H_2O \rightarrow H^+ + OH^-$). H^+ binds to functional groups while OH^- stabilizes at defect sites, forming a stable chemisorbed layer (Xing et al. 2021). With rising humidity, water molecules physically adsorb onto the chemisorbed layer via hydrogen bonding, gradually forming a continuous film within the porous structure. In this film, H^+ migrates rapidly via the Grotthuss proton-hopping mechanism ($H_2O + H_3O^+ \rightleftharpoons H_3O^+ + H_2O$), markedly boosting ionic conductivity and sensor response (Yang and Zhang 2024). Carbon defect sites further strengthen water adsorption affinity. Electrochemical impedance spectroscopy (EIS) was performed under varying humidity (Fig. 7b). The EIS curves showed near-linear behavior at 33–54% RH, indicating high impedance. As RH increased to 64–85%, the curves evolved toward a semicircular shape, reflecting enhanced ionic conductivity due to continuous water film formation. The humidity-dependent sensing performance of the CLN-X series was also evaluated (33–85% RH), as ambient humidity significantly influences sensor response (Wei et al. 2025). All materials showed increased response with RH (Figs. 7c, d and S8), with CLN-4 being the highest, followed by CLN-5, CLN-2, CLN-3, and CLN-1. CLN-3 exhibited notable signal fluctuations at 75% and 85% RH, consistent

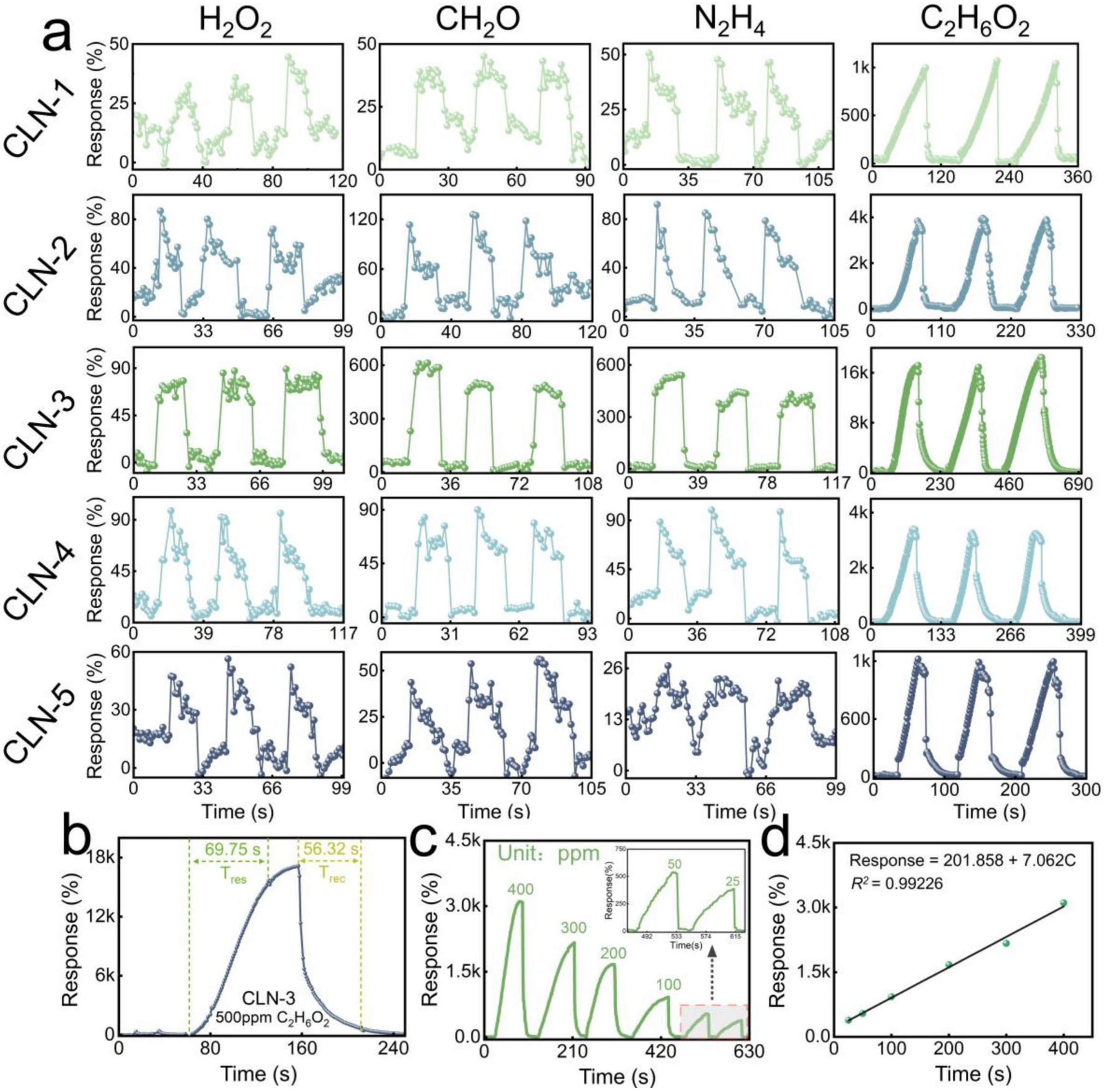

Fig. 5 Gas Sensing Performance of CLN-X Sensors: **a** Response curve of CLN-X; **b** Response time and recovery time of CLN-3 to 500 ppm EG; **c** CLN-3 at 25, 50, 100, 200, 300, 400 ppm; **d** Fitted curve

with the EIS results. CLN-X exhibits divergent humidity responses via the synergistic regulation of porous structure (specific surface area, pore volume) and surface oxygen species ($O_C/O_V/O_H$). CLN-3 maintains stable EG sensing under humidity variation through the optimal balance of these two factors (see Text S6 for detailed mechanism).

3.3 EG sensing mechanism of the CLN-3 sensor

Nanocellulose-derived biochar is a promising sensing material, featuring high surface area and porous structure that afford abundant adsorption sites. Our analysis reveals two synergistic factors underlying its high sensitivity and rapid response: hydrolysis time-tailored hierarchical porosity optimizing gas diffusion and active site access, and formed surface defects (e.g., oxygen vacancies) and functional groups promoting chemical adsorption. Their synergy optimizes mass transport and enhances surface activity, boosting gas capture and accelerating interfacial kinetics to underpin its superior sensing performance.

The gas sensing sensitivity of semiconductor materials is governed by two key factors: the charge depletion layer depth (L) and the particle size. Reducing the particle size while expanding L significantly enhances sensitivity

Table 1 Comparison of the sensing properties of this material with other reported sensing materials for EG

Sensing material	Temp.(°C)	Con. (ppm)	Res (%)	T_{res}/T_{rec} (s)	LoD (ppm)	Stability/Reproducibility (days/cycles)	Ref.
MoO_3	RT	500	7900	27/34	0.734	35/6	Liu et al. (2026)
ANDC/ZIF-8	RT	500	13,450	13.9/10.6	0.840	30/8	Zhu et al. (2025)
CMH	RT	500	15,540	14.2/37.3	0.292	30/3	Xu et al. (2025)
$CuO@Ga_2O_3$	160	100	3410	84/50	–	25/9	Geng et al. (2025)
SnO_2/ZnO	240	100	16,889	41/49	0.158	15/4	Dong et al. (2025a, b)
CuO/GO	110	10	3850	215/282	–	90/5	Lin et al. (2025)
BMO/In_2O_3	220	100	3700	26/129	1	60/5	Zhang et al. (2025)
$SmFeO_3$	180	100	11,600	80/95	–	12/6	Liu et al. (2023)
WO_3-400	160	100	230,400	137/321	1	30/5	Qu et al. (2024)
$Bi_{2-x}La_xFe_4O_9$	230	100	3750	39/256	0.0069	60/5	Zhao et al. (2025)
CLN-3	RT	500	17,576	69.7/56.3	0.360	40/10	This work

Response values herein are current-based percentage responses (higher = better). Literature data, originally R_a/R_g (R_a = air resistance, R_g = gas resistance; higher ratio = better), are converted to equivalent current-based percentage responses for consistent comparison. Both are common sensing performance metrics

(Epifani et al. 2008; Yamazoe and Shimanoe 2008), a relationship described by Eq. (1):

$$L \propto \sqrt{\frac{N_t^2}{N_d^2}} = \frac{N_t}{N_d} \tag{1}$$

The gas response relates to microstructural parameters through Eq. (2), where the areal density of chemisorbed oxygen ions (N_t) and the bulk carrier concentration (N_d) govern the depletion layer thickness (L) and grain size (D). Specifically, L increases with N_t and decreases with N_d. High oxygen coverage enhances electron capture, amplifying the response. At fiber junctions, the resistance follows an exponential barrier model, consistent with prior work (Xing et al. 2011).

$$R = R_0 \exp(\frac{qV}{kT}) \tag{2}$$

In this model, T is absolute temperature, κ the Boltzmann constant, R_0 a geometric prefactor, and qV the intergranular barrier height. Current depends exponentially on qV, so even a sub-100 meV change can alter resistance by an order of magnitude. The randomly stacked nanofibers of CLN-3 form a dense network of junctions, each with a similar barrier qV_1 that governs charge transport. Thus, the overall resistance R reflects the cumulative barrier across successive fiber–fiber interfaces. Upon air exposure, adsorbed oxygen extracts electrons to form O_2^- (Eqs. 3, 4) (Chwieroth et al. 2001; Xing et al. 2011; Yamazoe and Shimanoe 2008), introducing an additional barrier qV_2. This raises the total barrier to $q(V_1 + V_2)$, leading to a marked resistance increase (Song et al. 2023).

$$O_2(\text{gas}) \rightarrow O_2(\text{ads.}) \tag{3}$$

$$O_2(\text{ads.}) + e^- \rightarrow O_2^-(\text{ads.}) \tag{4}$$

Upon exposure to EG vapor (Fig. 8a), the molecules adsorb and oxidize with pre-adsorbed oxygen species (Eqs. 5, 6) (Zhu et al. 2025), releasing electrons back into the conduction band. This narrows the space-charge region and reduces resistance. The electron reinjection lowers the overall barrier height from $q(V_1 + V_2)$ to $q(V_1 + V_2 - V_3)$, markedly amplifying the sensor response.

$$(CH_2OH)_2(\text{gas}) \rightarrow (CH_2OH)_2(\text{ads.}) \tag{5}$$

$$2(CH_2OH)_2(\text{gas}) + 5O_2^-(\text{ads.}) \rightarrow 4CO_2 + 6H_2O + 5e^- \tag{6}$$

Additionally, the second sensing mechanism originates from the radial contraction of charge conduction pathways within the nanowire (Fig. 8b). The corresponding resistance (R) can be approximated using the nanowire resistance Eq. (7) (Miller et al. 2015):

$$R = 4\rho \frac{L}{\pi D^2{}_{\text{cond}}} \tag{7}$$

In this model, the resistance depends on the nanofiber's resistivity (ρ), length (L), and the diameter of its conductive core (D_{cond}). For the interconnected hollow nanofibers in CLN-3, D_{cond} is highly sensitive to the surface depletion layer depth. Chemisorption of oxygen expands this layer, reducing D_{cond} and thereby increasing the macroscopic resistance. To further elucidate the fundamental gas-sensing mechanism of the CLN-3 sensor, in situ

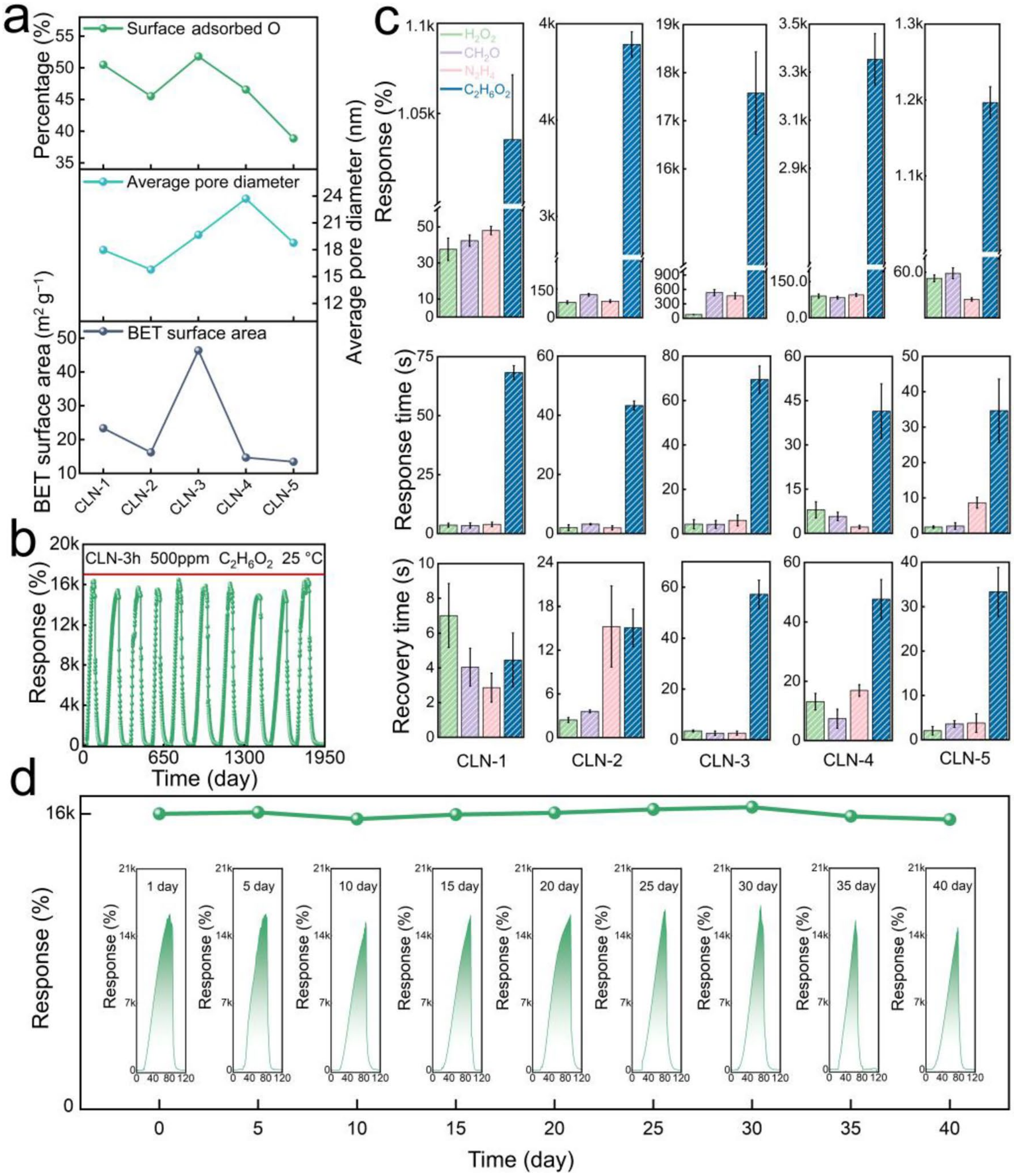

Fig. 6 **a** Surface adsorbed-oxygen ratio, average pore size, and BET surface area of the CLN-X series; **b** Cyclic stability of CLN-3 toward 500 ppm EG at 25 °C; **c** Selectivity, response time and recovery time of CLN-X sensor; **d** Long-term stability of CLN-3 sensor for 40 days

FTIR spectroscopy was used to monitor the interaction between CLN-3 and EG in real time. As shown in Fig. 8c, characteristic peaks appeared at 3465 cm^{-1} (O–H stretching of surface hydroxyl groups and/or adsorbed water) (Pradhan et al. 2020), 2973 cm^{-1} (C–H stretching of adsorbed EG), and ~ 2350 cm^{-1} (asymmetric stretching of CO_2). These spectral changes indicate that adsorbed EG is oxidized by surface oxygen species, ultimately producing CO_2 and H_2O (Zhao et al. 2025).

3.4 DFT calculations for elucidating the roles of Ca doping and adsorbed oxygen

To elucidate the roles of trace Ca doping and adsorbed oxygen, we conducted density functional theory (DFT)

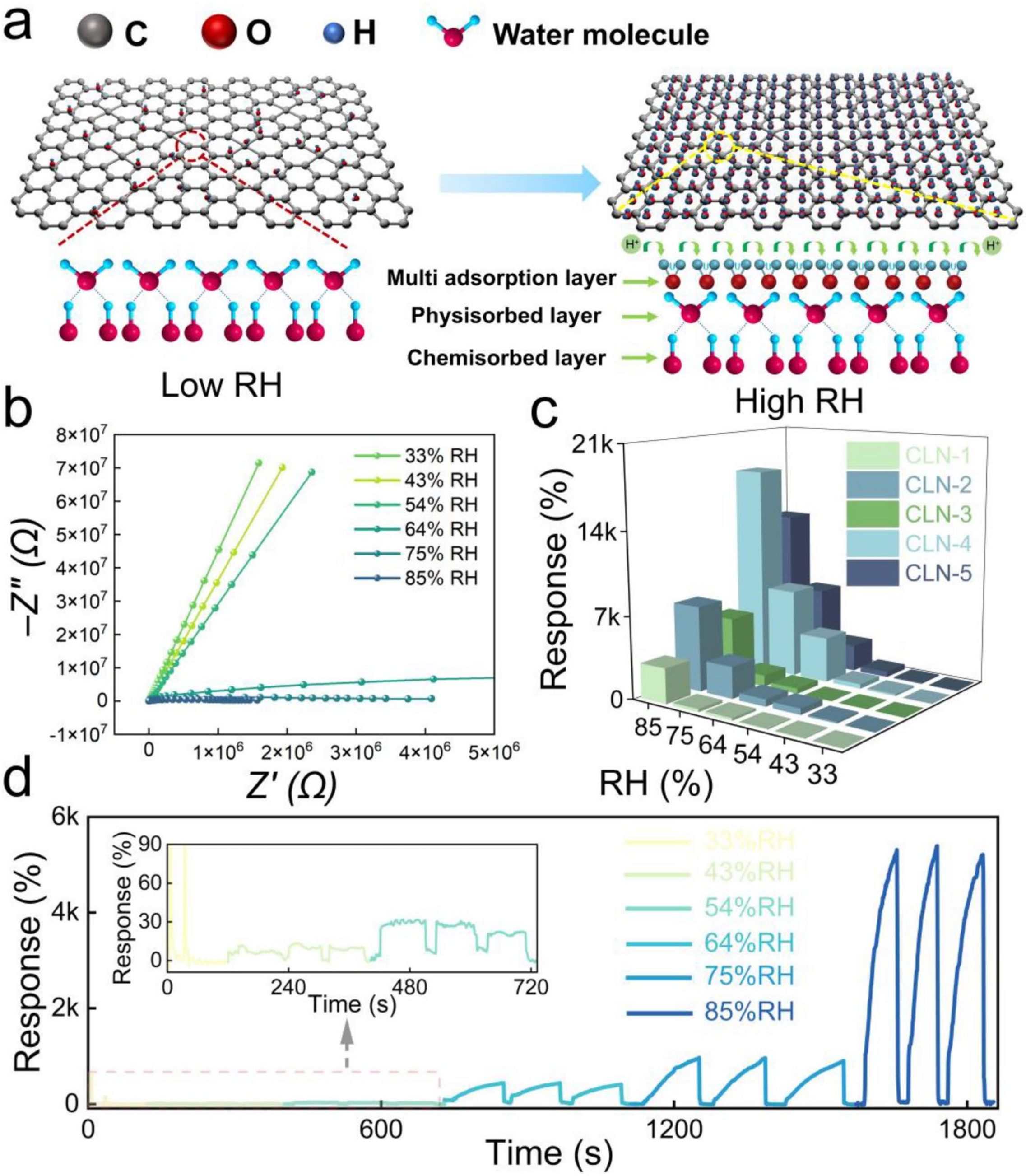

Fig. 7 **a** Schematic diagram of the humidity sensing mechanism of the CLN-3 sensor; **b** Nyquist plot of the CLN-3 material measured under 33–85% RH conditions; **c** Response distribution of CLN-1 to CLN-5 within the 33–85% RH range; **d** Dynamic response time curves of CLN-3 at different RH levels

calculations. After confirming the stability of defective bilayer graphene and Ca-doped models via ab initio molecular dynamics (AIMD), the gas adsorption properties were systematically evaluated. The adsorption energy ($E_{ads.}$) was calculated using Eq. (8):

$$E_{ads.} = E_{total} - E_{gas} - E_{substrate} \quad (8)$$

In this equation, E_{total} denotes the total energy of the system after gas adsorption, E_{gas} represents the energy of free gas molecules, and $E_{substrate}$ indicates the energy of the clean substrate. Charge density difference (CDD) analysis employs expression (9):

$$\Delta\rho = \rho_{total} - \rho_{substrate} - \rho_{gas} \quad (9)$$

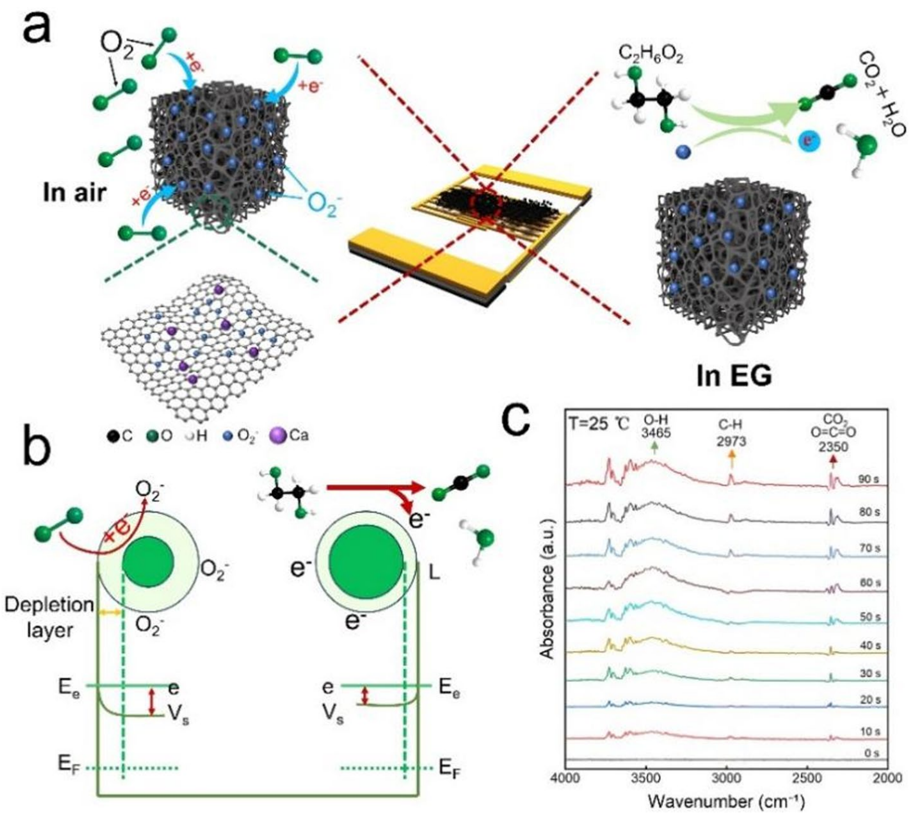

Fig. 8 Sensing mechanism schematic: **a** Surface reaction processes in different atmospheres; **b** Schematic of CLN-3 sensing mechanism; **c** In-situ infrared absorption spectrum of CLN-3 during EG exposure at 25 °C

In this expression, ρ_{total} corresponds to the total charge density following gas adsorption, $\rho_{\text{substrate}}$ refers to the charge density of the substrate alone, and ρ_{gas} denotes the charge density of an isolated gas molecule.

Computational results (Table 2, Figs. 9a, b and S9) show that calcium doping enhances the adsorption energy of O_2 from −0.03351 eV in the pristine structure to approximately −0.07062 eV, indicating that doping facilitates oxygen enrichment on the material surface. Furthermore, the adsorption energy of $C_2H_6O_2$ increases markedly from −0.13674 eV on the oxygen-pre-adsorbed surface to −0.39508 eV on the calcium-doped and oxygen-pre-adsorbed surface. This pronounced enhancement underscores the critical role of calcium doping in promoting $C_2H_6O_2$ adsorption (see Table 3 and Fig. 9c, d).

Quantitative insights from calculated adsorption energies (Table 3) reveal distinct $C_2H_6O_2$ adsorption behaviors on O_2^- pre-adsorbed substrates: the defective graphene bilayer exhibits weak physisorption of $C_2H_6O_2$ with an adsorption energy of −0.13674 eV, whereas the Ca-doped defective graphene bilayer shows stronger chemisorption ($E_{\text{ads.}} = -0.39508$ eV). These results confirm that Ca doping significantly enhances the affinity for $C_2H_6O_2$ on O_2^- pre-adsorbed surfaces, thereby improving the material' s gas-sensing performance. Complementary density of states (DOS) analysis (Fig. S10) further elucidates the underlying electronic mechanism. Upon O_2 adsorption, Ca doping introduces hybrid states near the Fermi level that strongly overlap with the C 2p and O 2p orbitals, enhancing electronic coupling at the O_2/substrate interface. For $C_2H_6O_2$ adsorption, the Ca-doped system displays broader and more overlapping contributions from Ca, C, and O states around the Fermi level, which improves orbital-coupling efficiency between the $C_2H_6O_2$ and the substrate. Together, the adsorption-energy calculations (Table 3) and DOS analysis demonstrate that the synergistic interface formed by Ca doping and pre-adsorbed oxygen promotes orbital hybridization,

Table 2 Adsorption energy of an O_2 molecule on undoped and Ca-doped defect bilayer graphite-like structures

System	$E_{\text{substrate}}$	E_{gas}	E_{total}	$E_{\text{ads.}}$ (eV)
Defective graphene bilayer	−518.00915	−9.91	−527.95267	−0.03351
Ca-doped defective graphene bilayer	−524.27031	−9.91	−534.25093	−0.07062

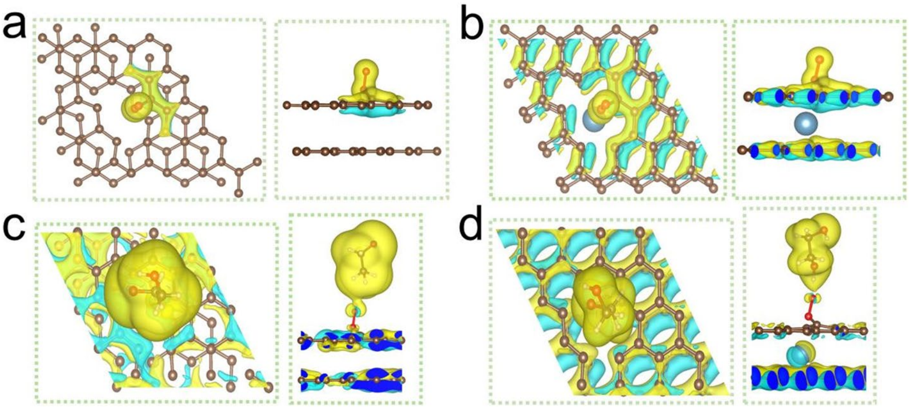

Fig. 9 Adsorption configurations and critical adsorption depths of O_2 molecules on uncalcium-doped and calcium-doped (**a**, **b**) surfaces, and $C_2H_6O_2$ molecules on uncalcium-doped surfaces adsorbing O_2 (**c**) and calcium-doped surfaces adsorbing O_2 (**d**)

thus enhancing both adsorption capacity and sensing response toward O_2 and $C_2H_6O_2$.

3.5 Practical application demonstration and limitations of the CLN-3 sensor

Figure 10a–c characterize the CLN-3 sensor's antifreeze detection performance: the concentration-dependent response to 1–5 mL antifreeze at 25 °C (inset: portable detection terminal), the integrated main control circuit, and the laboratory test setup for real-scenario simulation, respectively. These results verify the sensor's potential for antifreeze detection, but its practical application is limited by the gap between controlled laboratory conditions and complex real-world environments (variable backgrounds, temperatures, humidity, and antifreeze formulations), which may affect detection accuracy and stability. Field validation and targeted calibration are therefore required for reliable deployment in automotive and industrial settings.

4 Conclusions

Hydrolysis time is identified as the key regulator of pore structure and surface chemistry in nanocellulose-derived biochar. The optimally prepared CLN-3

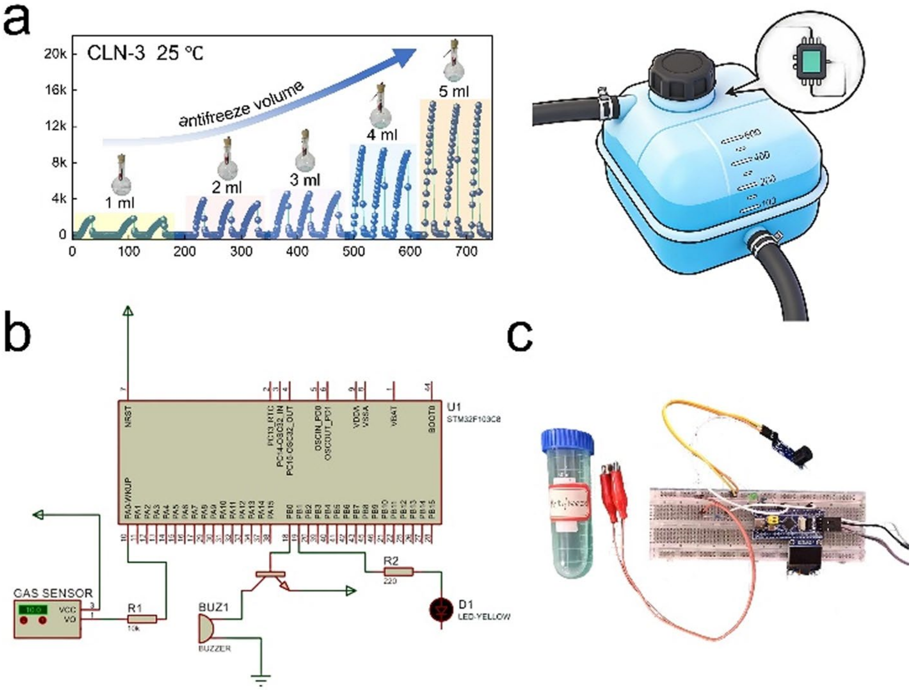

Fig. 10 **a** Response of the CLN-3 sensor to 1–5 mL of antifreeze (EG mass fraction ~ 50%) at 25 °C; **b** Circuit schematic; **c** Laboratory test setup

Table 3 The adsorption energy of a $C_2H_6O_2$ (EG) molecule on an oxygen-adsorbed defective graphene bilayer, and the adsorption energy on an oxygen-adsorbed, calcium-doped defective graphene bilayer

System	$E_{substrate}$	E_{gas}	E_{total}	$E_{ads.}$ (eV)
O_2-adsorbed on defective graphene bilayer	−529.18126	−53.40601	−582.72402	−0.13674
Ca-doped and O_2-adsorbed on defective graphene bilayer	−534.90894	−53.40601	−588.71004	−0.39508

exhibits a developed mesoporous network (46.36 m^2 g^{-1}), abundant oxygen vacancies, and exceptional EG sensing performance: a 17,576.67% response, a 0.36 ppm detection limit, and 40-day stability. DFT calculations reveal synergistic mechanisms involving hierarchical porosity for gas diffusion, oxygen vacancies/groups for charge transfer, and Ca doping for enhanced adsorbate coupling ($E_{ads.}$ from -0.13674 to -0.39508 eV). Moderate hydrolysis balances active sites and structural integrity. These findings establish a general defect/pore-regulation strategy, paving the way for cost-effective, sensitive, and adaptive VOC sensors for safety and environmental monitoring.

Supplementary Information

The online version contains supplementary material available at https://doi.org/10.1007/s42773-026-00624-w.

Supplementary material 1.

Acknowledgements

The authors gratefully acknowledge Professor Zhaofeng Wu of Xinjiang University for his guidance on the research design and manuscript revision. We also extend our thanks to Associate Professor Qihua Sun for her support with material characterization and theoretical calculations.

Author contributions

All authors contributed to the study conception and design. Yichen Gong and Cong Liang, who contributed equally to this work as co-first authors, together with Qihua Sun, Ping Hu and Yan Li, conducted material preparation, experiments and data collection. Junxi Cheng, Chang Liu and Bing Gao performed data analysis and investigation. Yichen Gong and Cong Liang drafted the manuscript. Zhaofeng Wu and Hua Zhuo supervised the project and secured funding. All authors commented on the manuscript drafts and approved the final version.

Funding

This work was financially sponsored by National Natural Science Foundation of China (No. 52563033), Natural Science Fund for Distinguished Young Scholars of Xinjiang Uygur Autonomous Region (Grant No. 2022D01E37), Key programs of Xinjiang Natural Science Foundation (Grant No. 2022B02051, 2024LQ01001-3, 2023B2045), Tianshan Talent Project of Xinjiang Uygur Autonomous Region (Grant No. 2024TSYCCX0007, 2023TSYCCX0109), Tianshan Talent Training Project-Xinjiang Science and Technology Innovation Team Program (Grant No. 2023TSYCTD0012), Research and Development of Biomanufacturing Technologies for the Lavender Industry (Grant No. 2024104140004).

Data availability

The datasets used or analyzed during the current study are available from the corresponding author upon reasonable request.

Declarations

Competing interests

The authors declare that they have no known competing financial interests or personal relationships that could have appeared to influence the work reported in this paper.

Author details

[1]School of Materials Science and Engineering, Xinjiang University, Urumqi 830046, Xinjiang, China. [2]Xinjiang Key Lab Solid State Phys & Devices, Urumqi 830046, Xinjiang, China. [3]Xinjiang Engineering Research Center for Environmental Functional Materials, Urumqi 830046, Xinjiang, China. [4]Xinjiang Uygur Autonomous Region Research Institute of Measurement & Testing, Urumqi 830000, China.

Received: 23 January 2026 Revised: 28 March 2026 Accepted: 24 April 2026

References

Antil B, Elkasabi Y, Strahan GD, Wal RLV (2025) Development of graphitic and non-graphitic carbons using different grade biopitch sources. Carbon 232:119770. https://doi.org/10.1016/j.carbon.2024.119770

Bai X, Hu P, Li A, Zhang Y, Li A, Zhang G, Xue Y, Jiang T, Wang Z, Cui H, Kang J, Zhao H, Gu L, Zhou W, Liu L, Qiu X, Guo L (2024) Nitrogen-doped amorphous monolayer carbon. Nature 634:80–84. https://doi.org/10.1038/s41586-024-07958-0

Biswas S, Rahaman T, Gupta P, Mitra R, Dutta S, Kharlyngdoh E, Guha S, Ganguly J, Pal A, Das M (2022) Cellulose and lignin profiling in seven, economically important bamboo species of India by anatomical, biochemical, FTIR spectroscopy and thermogravimetric analysis. Biomass Bioenergy 158:106362. https://doi.org/10.1016/j.biombioe.2022.106362

Chagas JS, Almeida JNS, Pereira ACL, Silva NFI, Raimundo RA, Medeiros ES, Lima B, Galvao LS, Santos ASF, Silva FI (2023) Evaluation of the kinetics of low intensity ultrasound-assisted sulfuric acid hydrolysis to obtain cellulose nanocrystals (CNCs) from microcrystalline cellulose (MCC). Cellulose 30:11455–11472. https://doi.org/10.1007/s10570-023-05580-3

Chaloupkova V, Ivanova T, Hutla P, Spunarova M (2021) Ash melting behavior of rice straw and calcium additives. Agriculture-Basel 11(12):1282. https://doi.org/10.3390/agriculture11121282

Chauhan AK, Singh SP, Rajpoot AS, Chauhan S, Meraj A, Jawaid M, Varghese E, Kumar V, Awad SA (2025) Preparation and applications of nanoparticles from lignocellulosic biomass: a review. Int J Biol Macromol 321(Part 1):146138. https://doi.org/10.1016/j.ijbiomac.2025.146138

Chen Y, Zhang X, Chen W, Yang H, Chen H (2017) The structure evolution of biochar from biomass pyrolysis and its correlation with gas pollutant adsorption performance. Bioresour Technol 246:101–109. https://doi.org/10.1016/j.biortech.2017.08.138

Cheng DL, Li T, Smith G, Yang J, Hang C, Miao ZY, Wu ZC (2019) Influence of calcium chloride impregnation on the thermal and high-temperature carbonization properties of bamboo fiber. PLoS ONE 14(2):e0212886. https://doi.org/10.1371/journal.pone.0212886

Choudhary M, Shrivastav A, Singh S, Sinha A, Krishnamurthy S, Mathur A, Wadhwa S (2025) Enhanced impedance-based detection of isoprene using carbon porous nanopowder (CPN) for early diagnosis of lung cancer. Mater Chem Phys 333:130381. https://doi.org/10.1016/j.matchemphys.2025.130381

Chwieroth B, Patton BR, Wang YZ (2001) Conduction and gas-surface reaction modeling in metal oxide gas sensors. J Electroceram 6:27–41. https://doi.org/10.1023/a:1011417619146

Copenhaver K, Li K, Wang L, Lamm M, Zhao X, Korey M, Neivandt D, Dixon B, Sultana S, Kelly P, Gramlich WM, Tekinalp H, Gardner DJ, MacKay S, Nawaz K, Ozcan S (2022) Pretreatment of lignocellulosic feedstocks for cellulose nanofibril production. Cellulose 29:4835–4876. https://doi.org/10.1007/s10570-022-04580-z

Dong H, Wei S, Chen W, Lu B, Cai Z, Yang B, Li X, Li X (2025a) Bioinspired lignocellulose foam: exceptional toughness and thermal insulation. ACS Nano 19(12):11712–11727. https://doi.org/10.1021/acsnano.4c11945

Dong J, Duan T, Shao TT, Li NJ, Guo JK, Zhang FC (2025b) Highly sensitive ethylene glycol gas sensor based on SnO_2/ZnO heterojunction composites. Vacuum 240:114503. https://doi.org/10.1016/j.vacuum.2025.114503

Eom Y, Son SM, Kim YE, Lee JE, Hwang SH, Chae HG (2019) Structure evolution mechanism of highly ordered graphite during carbonization of cellulose nanocrystals. Carbon 150:142–152. https://doi.org/10.1016/j.carbon.2019.05.007

Epifani M, Prades JD, Comini E, Pellicer E, Avella M, Siciliano P, Faglia G, Cirera A, Scotti R, Morazzoni F, Morante JR (2008) The role of surface oxygen vacancies in the NO_2 sensing properties of SnO_2 nanocrystals. J Phys Chem C 112(49):19540–19546. https://doi.org/10.1021/jp804916g

Ercan EET, Andreas L, Cwirzen A, Habermehl-Cwirzen K (2023) Wood ash as sustainable alternative raw material for the production of concrete-a review. Materials (Basel) 16(7):2557. https://doi.org/10.3390/ma16072557

Fang J, Li Z, Bai X, Wang D, Qie Y, Liu R (2024) Molecular adsorption behavior of O_2 molecules on Ni^{2+} doped TiO_2 (001) crystal plane. J Mater Sci Mater Electron 35:981. https://doi.org/10.1007/s10854-024-12723-0

Fang J, Hu P, Sun J, Ran B, Zheng W, Long Y, Wu Z, Duan H (2026) Biostructure-inspired high entropy carbon-like material derived from *Undaria pinnatifida* for room-temperature high-sensitivity hydrazine detection. Compos Part B Eng 309:113085. https://doi.org/10.1016/j.compositesb.2025.113085

Ferrari AC, Basko DM (2013) Raman spectroscopy as a versatile tool for studying the properties of graphene. Nat Nanotechnol 8:235–246. https://doi.org/10.1038/nnano.2013.46

Ferrari AC, Robertson J (2000) Interpretation of Raman spectra of disordered and amorphous carbon. Phys Rev B 61:14095–14107. https://doi.org/10.1103/PhysRevB.61.14095

Franklin RE (1951) Crystallite growth in graphitizing and non-graphitizing carbons. Proc R Soc Lond A Math Phys Sci 209(1097):196–218. https://doi.org/10.1098/rspa.1951.0197

Gao F, Zhang Y (2025) Effect and mechanism of coal desulfurization using a surfactant-assisted NaClO-NaOH system. Sci Rep 15:5116. https://doi.org/10.1038/s41598-025-88994-2

Geng W, Luan TY, Chen XR, Song PF, Duan LB, Qu FD, Cao AJ, Chen ZS (2025) High responsive ethylene glycol gas sensor based on CuO@Ga_2O_3 p-n hetero-junctions materials. J Alloys Compd 1038:182693. https://doi.org/10.1016/j.jallcom.2025.182693

Hayashi Y, Usami M, Ito ERD, Takeoka Y, Rikukawa M, Yoshizawa-Fujita M (2025) Effective synthesis of cationic cellulose with a high degree of substitution and its characteristics for battery applications. ACS Appl Polym Mater 7(5):3024–3032. https://doi.org/10.1021/acsapm.4c03671

Hernandez-Ortega J, Ahmed C, Molina A, Sabo RC, Cadena LES, Tenorio BA, Cabrera CR, Noveron JC (2025) High-performance catalytic oxygen evolution with nanocellulose-derived biocarbon and Fe/zeolite/carbon nanotubes. Catalysts 15(8):719. https://doi.org/10.3390/catal15080719

Holilah H, Bahruji H, Ediati R, Asranudin A, Jalil AA, Piluharto B, Nugraha RE, Prasetyoko D (2022) Uniform rod and spherical nanocrystalline celluloses from hydrolysis of industrial pepper waste (*Piper nigrum* L.) using organic acid and inorganic acid. Int J Biol Macromol 204:593–605. https://doi.org/10.1016/j.ijbiomac.2022.02.045

Hou Y, Han Z-M, Zhu Y, Xia J, Li J, Yang K-P, He Z, Song R, Guan Q-F, Lu Y, Yu S-H, Wu H (2025) Artificial kink defects enable high-efficiency degradation of nanocellulose via mechanochemical activation. Matter 8(9):102212. https://doi.org/10.1016/j.matt.2025.102212

Ibrahim RK, Hayyan M, AlSaadi MA, Ibrahim S, Hayyan A, Hashim MA (2019) Physical properties of ethylene glycol-based deep eutectic solvents. J Mol Liq 276:794–800. https://doi.org/10.1016/j.molliq.2018.12.032

Ike S, Wal RV (2024) Effect of carbonization methods on graphitization of soft and hard carbons. Carbon Trends 16:100382. https://doi.org/10.1016/j.cartre.2024.100382

Jin J, Ma H, Liang H, Zhang YY (2025) Biopolymer-derived carbon materials for wearable electronics. Adv Mater 37(22):2414620. https://doi.org/10.1002/adma.202414620

Kamboj R, Bains A, Goksen G, Dhull SB, Ali N, Khan MR, Chawla P (2025) Optimized pure cellulose from rice straw using low alkali concentration for sustainable nanocellulose and nanohydrogel production with enhanced dye reduction. Int J Biol Macromol 303:140364. https://doi.org/10.1016/j.ijbiomac.2025.140364

Lavarack BP, Griffin GJ, Rodman D (2002) The acid hydrolysis of sugarcane bagasse hemicellulose to produce xylose, arabinose, glucose and other products. Biomass Bioenergy 23(5):367–380. https://doi.org/10.1016/s0961-9534(02)00066-1

Li C, Han Y, Gao B, Tian N, Wu Z (2024) Biomimetic gas sensor derived from pine tree for highly sensitive and selective detection of $C_2H_6O_2$. Mater Chem Front 8(18):3053–3063. https://doi.org/10.1039/d4qm00442f

Li P, Li J, Jiannan LF, Shi J, Yu K, Xu H, Su F, Wang K, Li S, Zhang Y (2025) Ternary nanohybrids of MIL-125 derivatives (C-TiO_2) and Nano-Pd Dual-Hybridized polyaniline (PANI) for enhanced NH_3 gas sensing performance. ChemEng J 515:163425. https://doi.org/10.1016/j.cej.2025.163425

Lin J, Fu BY, Bi LY, Fu JX, Wen JS, Tian WY, Wang CJ, Wang Y (2025) Low temperatures and concentrations ethylene glycol sensing based on ultrathin graphene oxide-decorated CuO nanosheets. Microchem J 216:114542. https://doi.org/10.1016/j.microc.2025.114542

Liu M, Ma SY, Wang L, Cai YH, Ma NN (2023) Highly sensitive and selective glycol gas sensor based on $SmFeO_3$ microspheres. Ceram Int 49(1):1108–1113. https://doi.org/10.1016/j.ceramint.2022.09.086

Liu F, Chen Y, Qiu L, Zhang Z, Huang S, Liu T, Xie X, Ke J, Chen X, Ouyang YF (2025a) ZnO/activated carbon composites based gas sensor for flotation gases detection. Miner Eng 232:109562. https://doi.org/10.1016/j.mineng.2025.109562

Liu J, Wang X, Fan Z, Liu Z, Xu P, Sawant TR, Huang G, Deng X, Guo J, Wang J, Zhou M (2025b) Valorization of agricultural residues: challenges and opportunities in the production of bio-based materials. BioResources 20(2):4798–4820. https://doi.org/10.15376/biores.20.2.liu

Liu M, Ran B, Hu P, Fang J, Sun J, Bai Y, Ma Q, Ma X, Wu Z, Duan H (2025c) Room-temperature trimethylamine gas sensor with enhanced performance using biomass-derived carbon quantum dot modified biochar. J Environ Chem Eng 13(5):118427. https://doi.org/10.1016/j.jece.2025.118427

Liu M, Cheng J, Li Y, Sun Q, Wu Z (2026) Recycled MoO3 from spent HDS catalyst for efficient room-temperature detection of ethylene glycol. Chem Eng J 529:172591. https://doi.org/10.1016/j.cej.2026.172591

Long H, Harley-Trochimczyk A, Pham T, Tang Z, Shi T, Zettl A, Carraro C, Worsley MA, Maboudian R (2016) High surface area MoS_2/Graphene hybrid aerogel for ultrasensitive NO_2 detection. Adv Funct Mater 26(28):5158–5165. https://doi.org/10.1002/adfm.201601562

López EO, Bernardo PL, Checca NR, Rossi AL, Mello A, Ellis DE, Rossi AM, Terra J (2022) Hydroxyapatite and lead-substituted hydroxyapatite near-surface structures: novel modelling of photoemission lines from X-ray photoelectron spectra. Appl Surf Sci 571:151310. https://doi.org/10.1016/j.apsusc.2021.151310

Meunier V, Ania C, Bianco A, Chen Y, Choi GB, Kim YA, Koratkar N, Liu C, Tascon JMD, Terrones M (2022) Carbon science perspective in 2022: current research and future challenges. Carbon 195:272–291. https://doi.org/10.1016/j.carbon.2022.04.015

Miller DR, Akbar SA, Morris PA (2015) Nanoscale metal oxide-based heterojunctions for gas sensing: a review. Sens Actuators B Chem 211:569–569. https://doi.org/10.1016/j.snb.2015.02.086

Mohamed NB, Ngadi N, Rushdan AI, Yahya NY, Noor MHM, Inuwa IM, Opotu LA, Abu Bakar A, Ismail Y, Ali N (2025) Optimizing synthesis of anionic surfactant-modified carbon black for enhanced Ammonium adsorption. ChemNanoMat 11(1):e202400539. https://doi.org/10.1002/cnma.202400539

Mubari PK, Beguerie T, Monthioux M, Weiss-Hortala E, Nzihou A, Puech P (2022) The X-ray, Raman and TEM signatures of cellulose-derived carbons explained. C 8(1):4. https://doi.org/10.3390/c8010004

Pradhan S, Abdelaal AH, Mroue K, Al-Ansari T, Mackey HR, McKay G (2020) Biochar from vegetable wastes: agro-environmental characterization. Biochar 2:439–453. https://doi.org/10.1007/s42773-020-00069-9

Pratiwi H, Kusmono WMW (2023) Oxidized cellulose nanocrystals from durian peel waste by ammonium persulfate oxidation. ACS Omega 8(33):30262–30272. https://doi.org/10.1021/acsomega.3c03117

Qu X, Li MC, Mu HL, Jin BB, Song MG, Zhang KL, Wu YS, Li LS, Yu Y (2024) Facile fabrication of lilac-like multiple self-supporting WO_3 nanoneedle arrays with cubic/hexagonal phase junctions for highly sensitive Ethylene Glycol gas sensors. ACS Sens 9(7):3604–3615. https://doi.org/10.1021/acssensors.4c00600

Saupi FAC, Yusof NSM, Rajagopal V, Abd Rahman NMM (2025) Comparative analysis of nanocellulose extraction from *Cocos nucifera* shell by ultrasonication versus acid hydrolysis for Methylene Blue dye removal. Iran Polym J 34:1755–1778. https://doi.org/10.1007/s13726-025-01462-6

Sawatdee S, Botalo A, Pongchaikul P, Posoknistakul P, Phadungbut P, Intra P, Charnnok B, Chanlek N, Photongkam P, Laosiripojana N, Krisbiantoro PA, Wu KCW, Sakdaronnarong C (2025) Design of multilayer cellulose-based filters combined with Zeolitic Imidazole Framework and Silica nanoparticles for particulate matter filtration and antibacterial properties. ACS Sustain Chem Eng 13(19):7074–7087. https://doi.org/10.1021/acssuschemeng.5c00329

Shankar S, Rhim JW (2016) Preparation of nanocellulose from micro-crystalline cellulose: the effect on the performance and properties of agar-based composite films. Carbohydr Polym 135:18–26. https://doi.org/10.1016/j.carbpol.2015.08.082

Shi C, Qin H, Zhao M, Wang X, Li L, Hu J (2014) Investigation on electrical transport, CO sensing characteristics and mechanism for nanocrystalline$La_{1-x}Ca_xFeO_3$ sensors. Sens Actuators B Chem 190:25–31. https://doi.org/10.1016/j.snb.2013.08.029

Smith MW, Dallmeyer I, Johnson TJ, Brauer CS, McEwen JS, Espinal JF, Garcia-Perez M (2016) Structural analysis of char by Raman spectroscopy: improving band assignments through computational calculations from first principles. Carbon 100:678–692. https://doi.org/10.1016/j.carbon.2016.01.031

Smith-Craven MM, Dening TJ, Basra AK, Hageman MJ (2024) Enhanced dissolution of Amphotericin B through development of amorphous solid dispersions containing polymer and surfactants. J Pharm Sci 113(8):2454–2463. https://doi.org/10.1016/j.xphs.2024.04.031

Song J, Lin X, Ee L, Li SFY, Huang MH (2023) A review on electrospinning as versatile supports for diverse nanofibers and their applications in environmental sensing. Adv Fiber Mater 5:429–460. https://doi.org/10.1007/s42765-022-00237-5

Stan L, Volf I, Stan CS, Albu C, Coroaba A, Ursu LE, Popa M (2023) Intense blue photo emissive carbon dots prepared through pyrolytic processing of ligno-cellulosic wastes. Nanomaterials 13(1):131. https://doi.org/10.3390/nano13010131

Su C, Zhang L, Han Y, Ren C, Zeng M, Zhou Z, Su Y, Hu N, Wei H, Yang Z (2020) Controllable synthesis of heterostructured CuO-NiO nanotubes and their synergistic effect for glycol gas sensing. Sens Actuators B Chem 304:127347. https://doi.org/10.1016/j.snb.2019.127347

Sun Y, Lin L (2010) Hydrolysis behavior of bamboo fiber in formic acid reaction system. J Agric Food Chem 58(4):2253–2259. https://doi.org/10.1021/jf903731s

Sun Q, Xu Y, Wang W, Sun J, Li J, Li J, Wu Z, Duan H (2025) Room-temperature trimethylamine gas sensor with biomass carbon microtubule-grown SnO_2 nanosheets for efficient assessment of fish freshness. Ceram Int 51(19):27413–27422. https://doi.org/10.1016/j.ceramint.2025.03.414

Vinod A, Sanjay MR, Siengchin S, Fischer S (2021) Fully bio-based agro-waste soy stem fiber reinforced bio-epoxy composites for lightweight structural applications: influence of surface modification techniques. Constr Build Mater 303:124509. https://doi.org/10.1016/j.conbuildmat.2021.124509

Wang Y, Liu H, Ji X, Wang Q, Tian Z, Fatehi P (2023) Production of nanocellulose using acidic deep eutectic solvents based on choline chloride and carboxylic acids: a review. Int J Biol Macromol 245:125227. https://doi.org/10.1016/j.ijbiomac.2023.125227

Wang H, Kang H, Wang Z, Zhao J (2025a) Waste leaves into biomass carbon materials with tunable oxygen-containing functional groups for microwave absorption. Carbon 234:119930. https://doi.org/10.1016/j.carbon.2024.119930

Wang J, Zhang W, Liu Y (2025b) Thermochemical treatment of lignocellulosic biomass *Ceratophyllum demersum* at temperatures below 100 °C to prepare the carbon adsorbent. ACS Sustain Chem Eng 13(14):5394–5402. https://doi.org/10.1021/acssuschemeng.5c00826

Wei T, Ozbakir Y, Min H, Chen Y, Zheng H, Goel N, Gurin I, Bart S, Carraro C, Maboudian R (2025) Mitigating humidity interference in chemiresistive hydrogen sensors through hydrophobic surface functionalization. Sens Actuators B Chem 444(Part 1):138335. https://doi.org/10.1016/j.snb.2025.138335

Xing L, Yuan S, Chen Z, Chen Y, Xue X (2011) Enhanced gas sensing performance of $SnO_2/\alpha\text{-}MoO_3$ heterostructure nanobelts. Nanotechnology 22(22):225502. https://doi.org/10.1088/0957-4484/22/22/225502

Xing Y, Zhang LX, Xu H, Yin YY, Chong MX, Bie LJ (2021) Defect-rich ultrathin Sn_2O_3 nanosheets with dominant polar (100) facets for efficient gas and humidity sensor applications. Sens Actuators B Chem 349:130816. https://doi.org/10.1016/j.snb.2021.130816

Xu W, Zhang YY, Li MD, Qu FL, Poon CS, Zhu XH, Tsang DCW (2024) Durability and micromechanical properties of biochar in biochar-cement composites under marine environment. J Clean Prod 450:141842. https://doi.org/10.1016/j.jclepro.2024.141842

Xu Y, Sun QH, Li JL, Wu ZF, Duan HM (2025) High-performance ethylene glycol room-temperature gas sensor based on biomass-derived Na-doped porous carbon microtubules. Nanomaterials Basel 15(22):1686. https://doi.org/10.3390/nano15221686

Xue H, Zhang Y, Zhao Z, Gao H, Bao W, Li J, Zhang Z, Wang Q, He Q (2025) A review: sources, preparation and application of nanocellulose. J Polym Mater 42(2):379–409. https://doi.org/10.32604/jpm.2025.066695

Yahya AM, Adeleke AA, Nzerem P, Ikubanni PP, Ayuba S, Rasheed HA, Gimba A, Okafor I, Okolie JA, Paramasivam P (2023) Comprehensive characterization of some selected biomass for bioenergy production. ACS Omega 8(46):43771–43791. https://doi.org/10.1021/acsomega.3c05656

Yamazoe N, Shimanoe K (2008) Theory of power laws for semiconductor gas sensors. Sens Actuators B Chem 128(2):566–573. https://doi.org/10.1016/j.snb.2007.07.036

Yang C, Zhang HY (2024) Preparation and performance study of humidity sensor based on defect-controlled TiO_2/CdS heterostructure. Sens Actuators B Chem 404:135321. https://doi.org/10.1016/j.snb.2024.135321

Yang Z, Xiang M, Zhu W, Hui J, Qin H (2020) Biomass heteroatom carbon/cerium dioxide composite nanomaterials electrode for high-performance supercapacitors. ACS Sustain Chem Eng 8(17):6675–6681. https://doi.org/10.1021/acssuschemeng.0c00188

Yuan H, Aljneibi S, Yuan J, Wang Y, Liu H, Fang J, Tang C, Yan X, Cai H, Gu Y, Pennycook SJ, Tao J, Zhao D (2019) ZnO nanosheets abundant in oxygen vacancies derived from metal-organic frameworks for ppb-level gas sensing. Adv Mater 31(11):1807161. https://doi.org/10.1002/adma.201807161

Yuan H, Li NX, Fan WD, Cai H, Zhao D (2022) Metal-organic framework based gas sensors. Adv Sci 9(6):2104374. https://doi.org/10.1002/advs.202104374

Zhang Q, Yang LX, Li WK, Li XB, Liu XB, Sun S, Hu WY, Liu DN, Wang YJ, Ma SY (2025) Study of high-performance glycol gas sensor based on BMO/In2O3 heterostructure. Ceram Int 51(4):4661–4676. https://doi.org/10.1016/j.ceramint.2024.11.439

Zhao Y, Zhang X, Wang M, Meng L, Wang M, Hussain S, Qiao G, Liu G (2025) La-Doped mullite $Bi_2Fe_4O_9$ chemiresistive gas sensor for ultra-highly selective detection of Ethylene Glycol. Adv Mater 38(10):e17585. https://doi.org/10.1002/adma.202517585

Zhu Y, Sun Q, Liu M, Zhang W, Ran B, Hu P, Tian N, Sun J, Wu Z (2025) Novel gas sensor for ZIF-8 modified mould-derived carbon: for the detection of Ethylene Glycol at room temperature. Sens Actuators B Chem 443:138207. https://doi.org/10.1016/j.snb.2025.138207